REVIEW

This section of Journal of Materials Research is reserved for papers that are reviews of literature in a given area.

Overview: Damage in brittle layer structures from concentrated loads

Brian R. Lawn
Materials Science and Engineering Laboratory, National Institute of Standards and Technology, Gaithersburg, Maryland 20899

Yan Deng
Department of Materials and Nuclear Engineering, University of Maryland, College Park, Maryland 20742-2115

Pedro Miranda
Departamento de Electrónica e Ingeniería Electromecánica, Escuela de Ingenierías Industriales, Universidad de Extremadura, 06071 Badajoz, Spain

Antonia Pajares
Departamento de Física, Facultad de Ciencias, Universidäd de Extremadura, 06071 Badajoz, Spain

Herzl Chai
Department of Solid Mechanics, Materials and Systems, Faculty of Engineering, Tel Aviv University, Tel Aviv, Israel

Do Kyung Kim
Department of Materials Science and Engineering, Korea Advanced Institute of Science and Technology, Yusong, Taejon 305-701, Korea

(Received 12 April 2002; accepted 10 September 2002)

In this article, we review recent advances in the understanding and analysis of damage initiation and evolution in laminate structures with brittle outerlayers and compliant sublayers in concentrated loading. The relevance of such damage to lifetime-limiting failures of engineering and biomechanical layer systems is emphasized. We describe the results of contact studies on monolayer, bilayer, trilayer, and multilayer test specimens that enable simple elucidation of fundamental damage mechanics and yet simulate essential function in a wide range of practical structures. Damage processes are observed using *post mortem* ("bonded-interface") sectioning and direct *in situ* viewing during loading. The observations reveal a competition between damage modes in the brittle outerlayers—cone cracks or quasiplasticity at the top (near-contact) surfaces and laterally extending radial cracks at the lower surfaces. In metal or polymeric support layers, yield or viscoelasticity can become limiting factors. Analytical relations for the critical loads to initiate each damage mode are presented in terms of key system variables: geometrical (layer thickness and indenter radius); material (elastic modulus, strength and toughness of brittle components, hardness of deformable components). Such relations provide a sound physical basis for the design of brittle layer systems with optimal damage thresholds. Other elements of the damage process—damage evolution to failure, crack kinetics (and fatigue), flaw statistics, and complex (tangential) loading—are also considered.

I. INTRODUCTION

Laminate structures are often formed with brittle outerlayers (typically hard ceramics) to shield soft or compliant supporting underlayers or interlayers (metals, polymers, or even soft ceramics) from potentially deleterious external forces. Brittle outerlayers may also provide essential function, e.g., wear, corrosion, and thermal and electrical resistance. This notion of a protective outerlayer is a critical aspect of many engineering laminate structures, cutting tools, thermal barriers coatings (engine components), ceramic armor, laminated windows, eye glasses, and electronic packaging devices, to name a few [e.g., Fig. 1(a)]. It is especially crucial in biomechanical systems—natural structures, such as

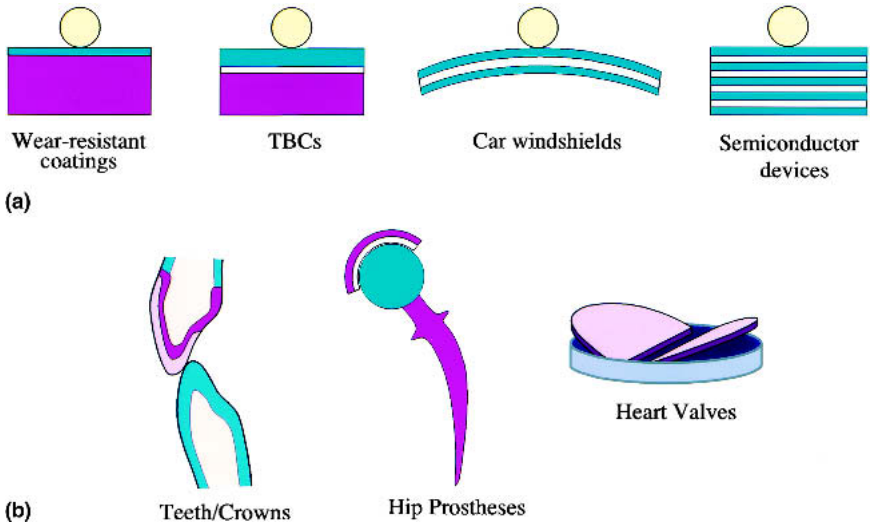

FIG. 1. Schematic showing laminate structures with brittle outer coating layers: (a) engineering structures; (b) biomechanical structures. These systems are especially susceptible to contact damage.

shells and teeth, and artificial structures, such as dental crowns, hip prostheses, and heart valves [Fig. 1(b)]—where biocompatibility, chemical durability, and even aesthetics are primary issues. Layer systems may consist of several different material types, ceramic, metal, polymer, and composite. Ceramics require particular attention because they can lead to premature cracking; they are commonly (although not exclusively) the principal source of failure in functional multicomponent structures. It is therefore important to understand the material and geometrical factors that limit the lifetimes of ceramic-based layer structures.

Of particular interest is the stress state imposed on such structures by concentrated loads, from contact or impact forces. Such loads present a worst case because local stresses can reach uncommonly high levels at relatively low applied loads.[1,2] When the contact radius remains small compared with the outerlayer thickness, concentrated loads can also induce flexural and other subsidiary stress states in the stiff outerlayers on their soft underlayer supports. This tends to be the case in thick coating systems ($\gg 1$ μm) in contact with millimeter-scale spherical indenters, up to and beyond the elastic limit of the structures.[3] Cracking and damage modes associated with these various stress states have been documented, some quite unique to contact loading: in the brittle outerlayers, cone or ring cracking and "quasiplasticity" at the upper surfaces[2,4] and radial cracking at the lower surfaces;[5–15] in the soft underlayers, plasticity (or quasiplasticity),[7,13,16] or even viscosity.[17] (These modes will be described in some detail in Sec. II. A.) While all modes can contribute to the demise of the laminate, radial cracks are a particular threat because they can initiate and spread laterally at comparatively low loads and can be difficult to detect in opaque coatings. A somewhat different state of affairs prevails when the contact exceeds the coating thickness, in which case the coating fails by a series of concentric transverse cracks beneath the indenter.[18–21] This latter case is commonly investigated in the context of thin films (<1 μm) in large contacts ($\gg 1$ μm) and will not be a focus of our attention here.

An important element of our study is the distinction between the philosophies of "crack containment" and "crack prevention". The first philosophy is important in large engineering structures where continual damage accumulation and energy absorption is tolerable and sometimes even desirable (e.g., ceramic armor). This is the traditional basis of structural design and is in evidence in natural shell structures.[22,23] Containment is achieved by enhancing crack deflection along weak interlayer interfaces to increase composite toughness,[24–26] by introducing residual compressive stresses into the ceramic layers to suppress transverse fracture,[27,28] or by incorporating tough sublayers to arrest any penetrant cracks.[6,7,27,29–32] Crack prevention is appropriate to small-scale structures where it is necessary to maintain high strength at all cost; e.g., dental crowns[33–38] and hip joint prostheses[39,40] that must withstand intense biting or body-weight forces under exacting *in vivo* environmental and cyclic conditions. The onset of any damage initiation could be potentially fatal to the intended function, particularly to fatigue life. While acknowledging the merits of both strategies, we focus especially here on the more conservative approach of prevention, because of its relevance to biomechanical prostheses and advanced material devices.

In this article, we survey results of basic studies on a variety of laminate structures with brittle ceramic outerlayers. Although we draw mainly from our own studies for illustrative examples, using model layer systems, the subject matter is considered in a broader context. The test of choice is that of normal Hertzian contact with a sphere indenter on the top surface of a flat-layer specimen. This

test lends itself to uniquely simple and reproducible experimentation, is amenable to explicit fracture mechanics and damage analysis, and is representative of a wide range of practical configurations. We present examples of damage incurred within a variety of layer systems, observed indirectly by routine sectioning or directly using novel *in situ* experimentation. First, damage modes in component monolithic brittle materials are briefly described. Then we consider simple bilayers, fabricated from the same monolithic brittle materials as coating layers bonded onto soft substrates. Finally, we consider trilayers and multilayers. The evolution of the basic damage modes, from initiation to final failure, is described for each structural type. Explicit analytical relations for the critical loads to produce each form of damage are presented, in terms of basic material quantities (modulus, strength, toughness, and hardness) and geometrical variables (layer thickness, contact radius). These relations may be used to establish guidelines for designing optimal layer structures for specific applications and to provide a rational basis for ensuing analysis of more complex layer structures, e.g., geometrically convoluted dental crowns and hip prostheses.

II. MONOLITHS

A principal goal of our approach is to be able to predict the contact damage responses of layer structures from basic properties of the constituent monolithic materials. Values of Young's modulus, hardness, toughness, and strength for selected case study materials are appropriately listed in Table 1.[13,15,41–43] These listed values are subject to variation depending on microstructural characteristics and should be considered as no more than representative of each material.[44] Toughnesses and strengths for metals and polymers are omitted because those materials are generally not susceptible to fracture in ceramic-based layer systems. Other unlisted parameters may be required in more detailed analyses: crack velocity exponents for ceramics; Poisson's ratio and strain-hardening coefficients for all materials (determinable from indentation stress–strain curves[9,45]); viscoelasticity parameters for polymers.

A. Contact damage modes

Surface-contact damage modes in ceramic monoliths are of interest because they persist in ceramic-based multilayers. A brief description of these modes is presented here. The reader is referred to previous articles for more detail.[2,4,44,46]

Consider indentation on a ceramic surface by a sphere of radius r_i at normal quasistatic load P over a contact radius a (Fig. 2). The Hertzian stress field contains a large component of hydrostatic compression, considerable shear, and modest tension.[1,2,4,46] For general purposes, it is useful to define an "effective radius" by $1/r = 1/r_c + 1/r_i$ and "effective modulus" by $1/E = 1/E_c +$

TABLE I. Properties of representative materials.[a]

Material	Modulus E (GPa)	Hardness H (GPa)	Toughness T (MPa $m^{1/2}$)	Strength σ (MPa)
Ceramic				
Glass (abraded)	73	5.2	0.7	110
Sapphire (abraded)	417	21	3.0	550
Silicon (abraded)	170	14	0.7	110
Porcelain (dental)	68	6.2	0.9	110
Alumina (dense, fine grain)	390	20	3.1	620
Alumina (glass-infiltrated)	270	12.3	3.0	550
Zirconia (Y-TZP)	205	12.0	5.4	1450
Zirconia (glass-infiltrated)	245	13.1	3.5	440
Mica glass–ceramic (F-MGC)	70.5	3.8	1.0	325
Mica glass–ceramic (C-MGC)	51.5	2.7	1.7	125
Glass–ceramic (lithium disilicate)	104	5.5	2.9	420
Metal				
Aluminum	71	0.77		
Steel	199	1.8		
Pd–alloy (dental)	126	2.0		
Co–alloy (dental)	231	3.0		
Tungsten carbide (indenter)	614	19		
Polymer				
Glass-filled polymer (dental)	10	0.8		
Polycarbonate	2.3	0.3		
Epoxy	3.5	0.4		
Tooth				
Enamel	94	3.2	0.8	
Dentin	16	0.6	3.1	

[a]Data from Refs. 13, 15, and 41–43.

$1/E_i$,[47] with subscripts c and i referring to ceramic and indenter materials, respectively. Special cases of interest are the following: a rigid sphere on a flat specimen, $r = r_i$ and $E = E_c$ (simple test configuration, Fig. 2); two like contacting spheres, $r = r_c/2$ and $E = E_c/2$ (dental crowns). Hence, one can use data from simple test configurations to predict the response of more complex curved-surface geometries. The methodology is also readily extendable to sliding, rotational, and cyclic loading.[2]

Beyond a critical contact load, irreversible damage forms in the ceramic specimen (sometimes also in the indenter). This damage can manifest itself either as classical cone cracking in response to the tensile stresses (C = brittle response) or a form of yield deformation in response to the shear stresses (Y = quasiplastic response).[2,4] Figure 3 illustrates damage patterns for two micaceous glass–ceramics with the same composition but with fine (F-MGC) and coarse (C-MGC) grain microstructures.[48] The micrographs are half-surface and side views from bonded-interface specimens in which the specimens are first cut into two halves, rejoined with adhesive or screws, indented along the bonded interface trace, and finally reseparated for side viewing.[49,50] In F-MGC [Fig. 3(a)], the predominant form of damage is cone cracking. Cone cracks pop in unstably from an embryonic surface flaw once the associated stress intensity factor exceeds the material toughness, and thereafter grow stably with increasing load. In C-MGC [Fig. 3(b)], the damage takes the form of a quasiplastic zone. Quasiplasticity in ceramics is macroscopically analogous to plasticity in metals (viscoplasticity in polymers) but is fundamentally different microscopically, consisting of sliding shear faults at weak grain, interphase, or twin boundaries. These shear faults initiate above a well-defined yield stress, determined by an internal friction or cohesive stress at the sliding interfaces.[51–54] Because it is these same internal friction mechanisms that are responsible for *R*-curve behavior, a correlation exists between susceptibility to quasiplasticity and toughness in ceramics.[44] Such brittle–ductile transitions with increasing microstructural heterogeneity are typical of all polycrystalline ceramics, including glass–ceramics,[55] alumina,[49,56] silicon carbide,[57] silicon nitride,[58] and zirconia.[59]

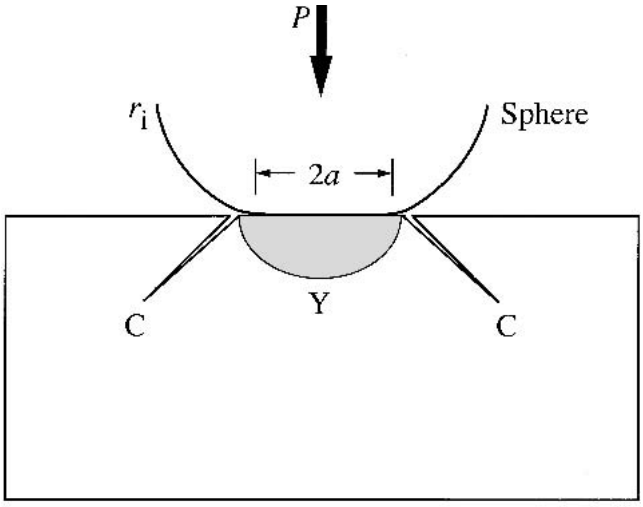

FIG. 2. Schematic of contact test with sphere of radius $r = r_i$ at load *P*, contact radius *a*, on flat monolithic specimen. Damage may occur by cone cracking C (brittle mode) or by yield Y (plastic or quasiplastic mode).

Both cone cracks and quasiplasticity can lead to strength loss in ceramic components, the latter from microcrack formation at the ends of the shear faults.[51,53,55,59–63] Both modes are susceptible to fatigue, especially in cyclic loading and moist environments, cone cracks from slow crack growth[64,65] and quasiplasticity from cumulative mechanical degradation of the sliding internal interfaces, leading to coalescence into dangerous radial macrocracks.[63] It follows that quasiplastic ceramics are also highly susceptible to surface removal and wear processes.[66–68]

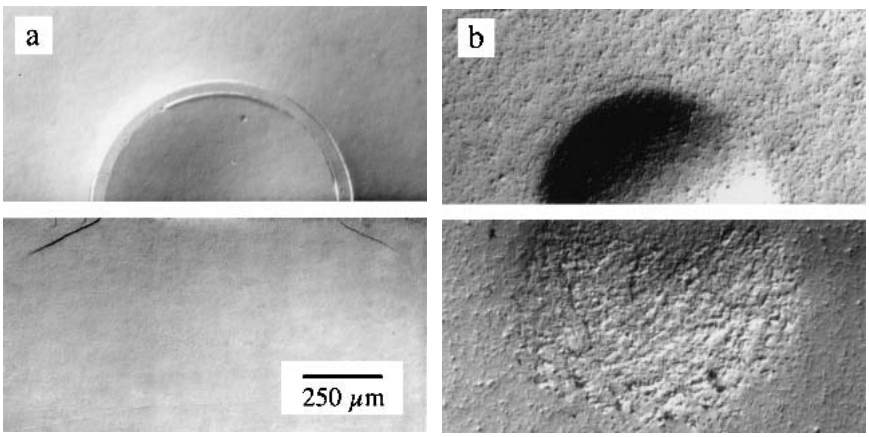

FIG. 3. Damage in micaceous glass–ceramics (a) fine-grain (F-MGC) and (b) coarse grain (C-MGC), from indentation with WC sphere of radius $r = 3.18$ mm at $P = 1000\,N$. Upper micrographs are half-surface views and lower micrographs side views, from bonded-interface specimens.

B. Fracture and deformation mechanics

Analytical modeling of cone cracks[2,46,69] (C) and quasiplasticity[47] (Y) enables derivation of explicit relations for the corresponding critical contact loads:

$$P_C = A(T^2/E)r \quad , \tag{1a}$$

$$P_Y = DH(H/E)^2 r^2 \quad , \tag{1b}$$

with E the effective Young's modulus, T the toughness (K_{IC}), H the hardness, and A and D dimensionless coefficients (usually calibrated against experimental data for well-documented materials).[47] The appearance of T in Eq. (1a) and $H \approx 3Y$[45,47,70] in Eq. (1b) reflects the underlying fracture and yield processes described in the previous subsection. Note the different dependence on sphere radius r in Eqs. (1a) and (1b). Clearly, it is desirable to avoid sharp contacts, i.e., keep r large, to minimize damage from either mode. At $P > P_C$, cone cracks expand stably with increasing load according to Roesler's relation for pennylike cracks ($c \propto P^{2/3}/T$), independent of r.[46,71,72] An analogous dependence of quasiplastic zone size with increasing load at $P > P_Y$ has thus far been studied only by numerical analysis.[9]

The above formulation quantifies the competition between the two modes. Comparing Eqs. (1a) and (1b) yields $P_Y/P_C = (D/A)(H/E)(H/T)^2 r$, which may be taken as a brittleness index for any specified indenter size r. The appearance of H/E and H/T as controlling material factors is commonplace in indentation theory.[73–75] In metals and polymers, and also in a wide range of heterogeneous ceramics, $P_Y/P_C < 1$ for spheres in the common contact testing range r = 1–10 mm;[38,47] only a select few fine-grain or glassy ceramic materials, e.g., silicon and silicate glasses, favor cone cracking in this range.

III. BILAYERS

Now consider bilayers consisting of ceramic plates of thickness d bonded to a substrate support (Fig. 4). The same local Hertzian stress states responsible for cone cracking and quasiplasticity described in Sec. II persist at the near-contact regions in the ceramic top surface. However, mismatch between layer components can induce new stress states in the ceramic coating, most notably from flexure on a compliant or soft base. These latter stresses become dominant as the coating becomes thinner (but not too thin that $d \ll a$ in Fig. 4, in which case membrane stresses become dominant[20,21]). Coating flexure can modify the critical conditions in Eq. (1). An even greater consequence is the generation of subsurface radial cracks (R) within a bell-shaped distribution of tensile stresses at the coating undersurfaces. These radial cracks are somewhat similar in geometry to those generated from quasiplasticity zones in monoliths, although the stress field driving them is quite different. Flexural radial cracks have been identified as a primary source of failure in all-ceramic dental crowns.[37]

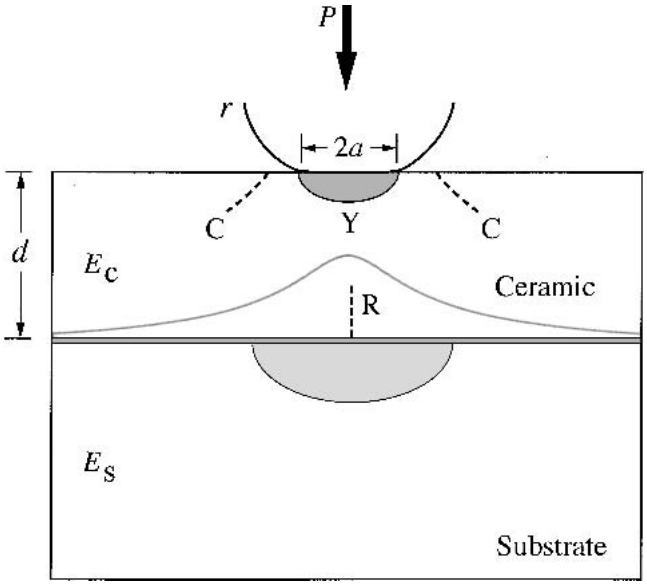

FIG. 4. Schematic of contact test with sphere on bilayer specimen with brittle coating, thickness *d.* Surface cone cracking C and yield Y are as in monoliths (Fig. 2). Radial crack (R) initiates at lower coating surface, in bell-shaped tensile region. Yield may also occur in soft substrate.

A. Radial cracking: Bonded-interface specimens

The basic nature of damage patterns in brittle ceramic coatings from surface-concentrated loads has been elucidated in a wide range of bilayer structures, using bonded-interface section specimens: all-ceramic systems such as alumina/alumina,[6,32,76] glass/glass–ceramic,[7] and silicon nitride/silicon nitride;[11,12,31] thermal barrier coatings;[8,9,16,77,78] simulated dental structures.[13] Selected examples are shown in Fig. 5, for indentation with WC spheres of radius r = 2–4 mm: (a) F-MGC [recall Fig. 3(a)] bonded with dental cement to a filled-polymer composite substrate (simulating tooth enamel/dentin);[13] (b) porcelain fused to Pd–alloy metal;[79] (c) glass fused to C-MGC [recall Fig. 3(b)];[7] (d) porcelain fused to a dental glass-infiltrated alumina.[13] Figure 6 maps corresponding tensile stresses (contours of normal stresses perpendicular to the radial crack plane) in the elastic coatings and any yield zones (boundaries of von Mises stress = yield stress) in soft substrates, from finite element modeling (FEM) using data in Table I.[13]

In all four illustrative examples cone cracks remain in evidence at the coating top surface, and radial cracks are apparent in the first three. In Figs. 5(a) and 6(a), the ceramic coating "shields" the low-modulus polymeric substrate from the applied loading (although the deformation is not entirely elastic). The associated coating flexure induces high tensile stresses at the undersurface, promoting radial cracks, and simultaneously shifts the

maximum surface tensile stress on the top surface from the contact to the outer shoulders, expanding the diameter of the surface ring cracks.[80] (The appearance of such expanded ring cracks at the top surface can be a valuable indicator of the existence of subsurface radial cracks in unsectioned specimens.[81]) In Figs. 5(b) and 6(b), the Pd–alloy substrate is actually stiffer than the porcelain coating but is softer (Table I). Flexure in this case is thus enabled by local yield in the metal support, leading once more to radial cracking. In Figs. 5(c) and 6(c), the C-MGC substrate has stiffness similar to that of the glass coating but once more is softer, emphasizing the potentially critical role of quasiplasticity in the radial cracking process. Finally, in Figs. 5(d) and 6(d), no radial cracking is evident at all, since the alumina substrate is both stiffer and harder than the porcelain, suppressing any tensile stresses at the coating undersurface [Fig. 6(d)].

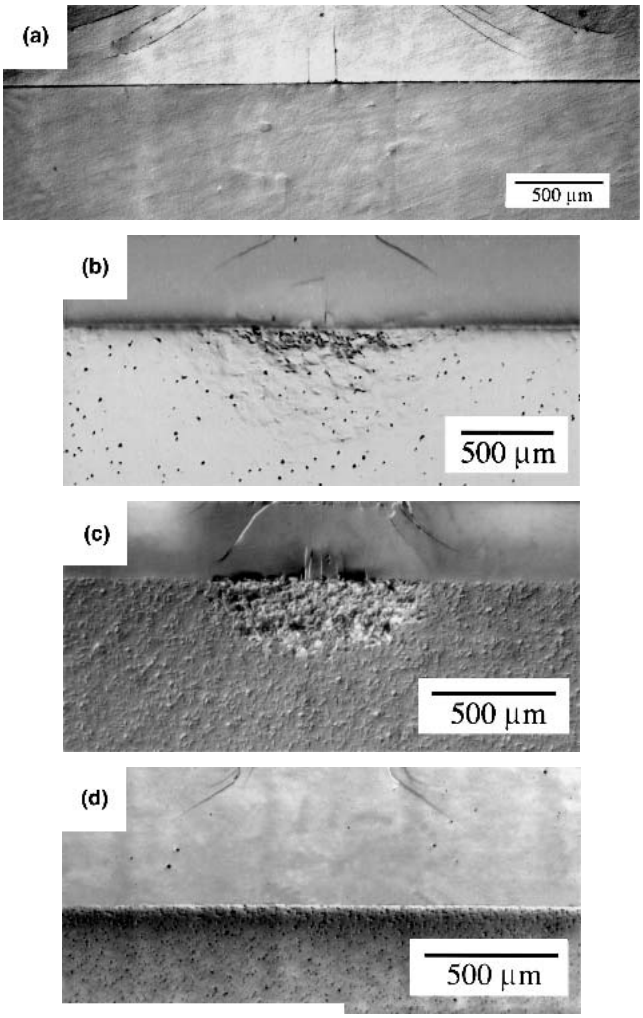

FIG. 5. Section views of damage in flat ceramic-coating/substrate bilayers: (a) F-MGC/filled-polymer, WC sphere indenter $r = 3.18$ mm at $P = 250$ N;[13] (b) porcelain/Pt–alloy, $r = 2.38$ mm at $P = 500$ N;[79] (c) glass/C-MGC, $r = 3.18$ mm at $P = 350$ N;[7] (d) porcelain/glass-infiltrated-alumina, $r = 3.18$ mm at $P = 500$ N.[13] Bonded-interface specimens are used.

Thus a prescription for improved performance on ceramic-based bilayers would appear to be a stiff and hard substrate support. As we shall see in Sec. IV, this conclusion does not necessarily carry over to trilayers. Interestingly, delamination is not observed to be a primary factor in the ceramic-based bilayers, even where the interlayer bond is weak [e.g., Fig. 5(a)], (except in the final stages of contact damage when a substrate yield zone becomes large relative to the coating thickness).[8,14]

B. Radial cracking: Model layer systems

Sectioning experiments of the kind represented in Fig. 5, while informative, can be cumbersome. They do not reveal full geometrical features of the radial crack patterns or how these cracks evolve to failure. Most

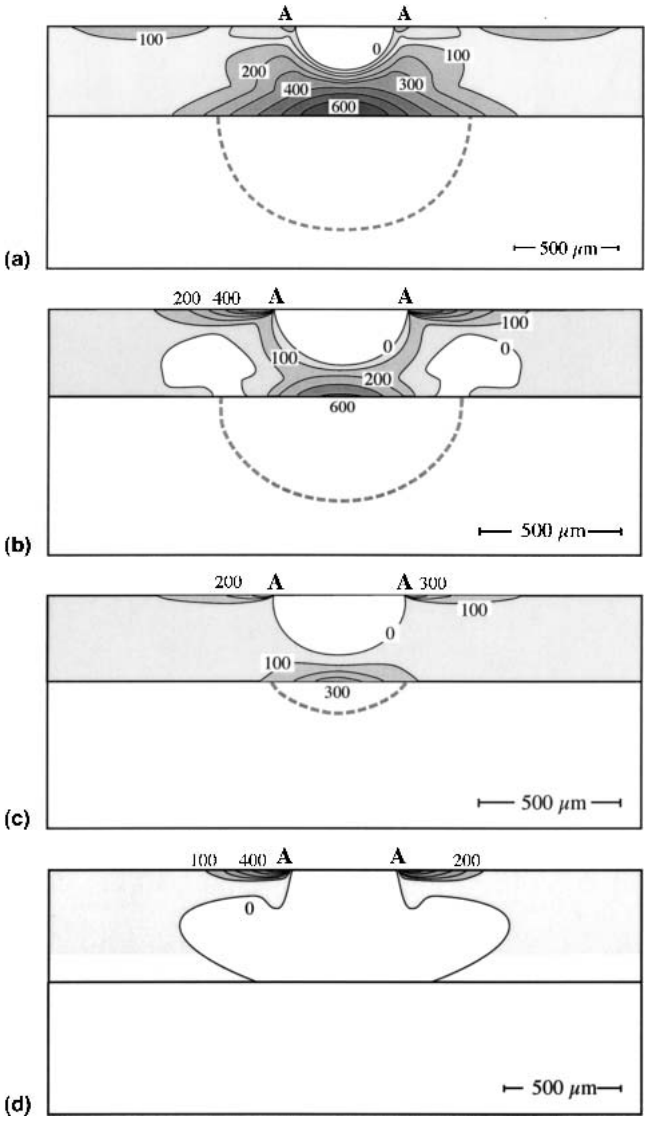

FIG. 6. FEM-generated tensile stress contours in brittle coating corresponding to examples in Fig. 5 (solid curves). Yield zone in substrate is shown where applicable (dashed curves). AA is contact diameter, and contours are in units of MPa.

important, they do not lend themselves to straightforward determination of critical threshold loads and are thus not amenable to quantitative analysis. Elucidation of fracture mechanics requires a more direct experimental approach.

Tests on model bilayers fabricated from transparent components for *in situ* observation of crack initiation and propagation are proving useful in this regard.[10,41,80,82] Glass or sapphire coating layers are simply bonded to polycarbonate substrates with thin interlayers of epoxy adhesive. Cracking in the coating layer is monitored either from the side through the coating walls or from below through the substrate base during indentation. Several indentation tests can be carried out on a typical bilayer specimen of minimum lateral dimension 25 mm. Selective preabrasion treatments of the coating surfaces with abrasive grit[80] (or Vickers indentations[83]) provide controlled flaw states for preferential initiation of radial cracks at the bottom surface (or cone cracks at the top surface). Examples of radial cracks in glass coatings with preabraded lower surfaces bonded to polycarbonate bases are shown in Fig. 7. Figure 7(a) shows a side-on view of one radial crack (others are present but are inclined to the plane of view). Initiation has occurred at the glass undersurfaces, and the crack has spread laterally into an elongate configuration. Figure 7(b) displays a corresponding subsurface view (different specimen), showing a radial "star" pattern. The radial cracks pop in abruptly at threshold and thereafter multiply and spread stably with increasing load, remaining self-contained within the coating layer until failure occurs by through-thickness penetration.

The same *in situ* set up may be retained for bilayers with one opaque component, with some restrictions. For transparent brittle coatings on metal substrates, both cone and radial cracks can be viewed through the side walls.[42] For polycrystalline ceramic coatings on transparent substrates, radial cracks can still be viewed from below (cone cracks and quasiplasticity require *post mortem* examinations). Figure 8 is an example of the second kind, an alumina coating layer on a polycarbonate base, showing subsurface views of radial crack evolution through one complete loading/unloading cycle:[14] crack initiation [Fig. 8(a)], extension, and multiplication [Figs. 8(b)–(d)] and subsequent retraction and closure on unloading [Figs. 8(e) and 8(f)]. (The alumina surfaces in this case are polished—preabrasion is unnecessary because flaws are available from within the microstructure.) In comparable experiments on abraded (001) single-crystal coatings the radial cracks follow crystallographic traces of preferential cleavage planes, e.g., (111) planes in silicon.[43]

Typically, ceramic/polymer bilayer structures can sustain an increase in applied load of up to one order of magnitude between the onset of first radial cracking and final failure. Such damage tolerance is typical of composite

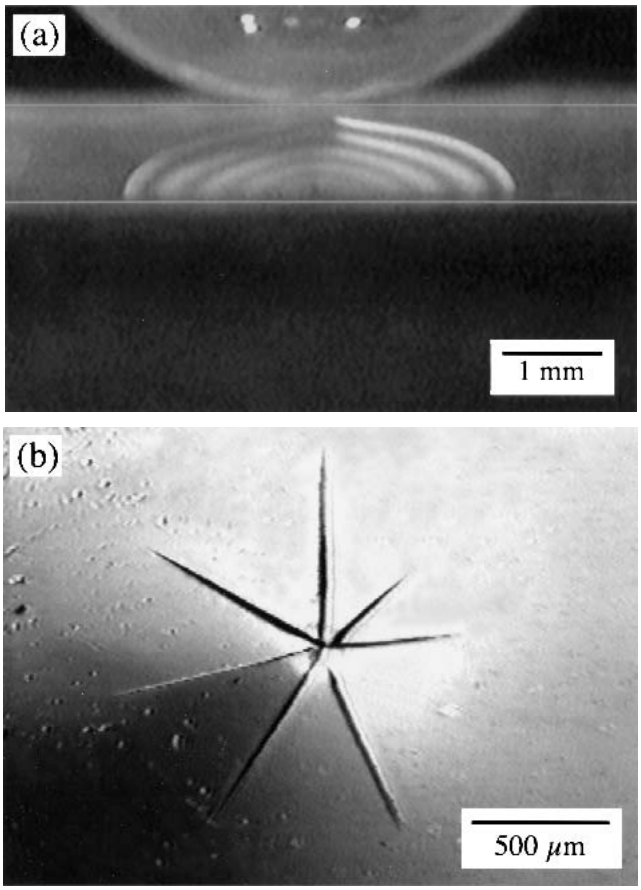

FIG. 7. Radial cracking in model glass/polycarbonate bilayers, from contact loading with WC sphere.[80] Glass bottom surfaces are preabraded. *In situ* views: (a) side, $d = 1$ mm, $P = 130$ N (fringes are from interference at open crack walls); (b) subsurface, $d = 230$ μm, $P = 31$ N.

structures. However, once cracking starts, it can signal the end of useful lifetime in many high-strength structures, so the critical load for onset of first damage is a useful, conservative design parameter.

C. Fracture mechanics: Elastic substrates

1. Basic relations

Suppose the deformation in the substrate remains perfectly elastic, so that all damage from the external contact is contained within the brittle coating. For thicker coatings where Hertzian stresses continue to dominate, we may expect Eqs. (1a) and (1b) to remain useful bounds for cone cracking (P_C) and quasiplasticity (P_Y), relatively independent of d (Fig. 4). For thinner coatings, flexural stresses become dominant, and radial cracks initiate at the tensile undersurface. (In this latter region the surface tensile stress concentrations at the top surface move away from the contact and diminish in intensity, inhibiting ring cracking.[80]) The maximum tensile stress at the center of the coating undersurface (Fig. 4)

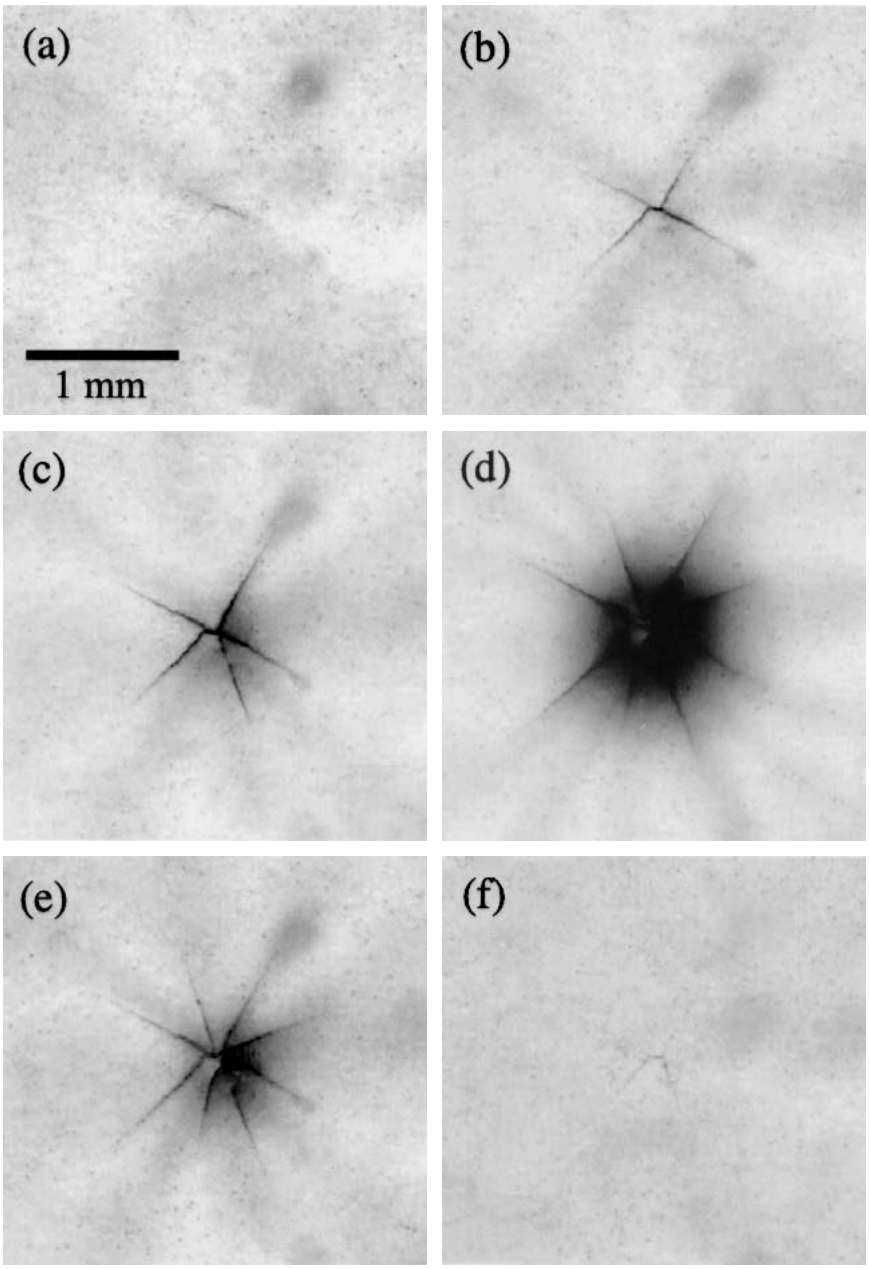

FIG. 8. Radial crack sequence in glass-infiltrated-alumina/polycarbonate bilayer, coating thickness $d = 155$ μm, from contact loading with WC sphere.[14] Lower alumina surface is as-polished. *In situ* subsurface views are shown. Loading half-cycle: (a) $P = 15.1$ N; (b) $P = 24.0$ N; (c) $P = 35.1$ N; (d) $P = 56.6$ N. Unloading half-cycle: (e) $P = 33.3$ N; (f) $P = 0$ N.

may be determined from the theory of plates on elastic foundations.[84] Equating this stress to the bulk flexural strength σ_c of the coating material ("critical stress" condition) yields the critical load for radial cracking,

$$P_R = B\sigma_c d^2/\log(CE_c/E_s) \quad , \qquad (2)$$

in the lower-bound approximation of point loading ($a \ll d$, Fig. 4), with B and C dimensionless constants (again usually calibrated against data for well-behaved material systems[14]). The quadratic dependence on d is typical of flexing plates. Strength σ_c and, to a lesser extent, modulus ratio E_c/E_s are the important materials variables. The appearance of σ_c confirms the importance of flaw state at the coating undersurface. Equation (2) remains an adequate approximation as long as the starting flaws remain small compared to coating layer thickness and are of sufficient density (see below). Note that P_R is independent of r in Eq. (2).

Critical load measurements are most readily made from *in situ* tests on model ceramic/polycarbonate bilayers (e.g., Figs. 7 and 8). Figure 9 plots critical load data for the onset of first damage in selected dental ceramic

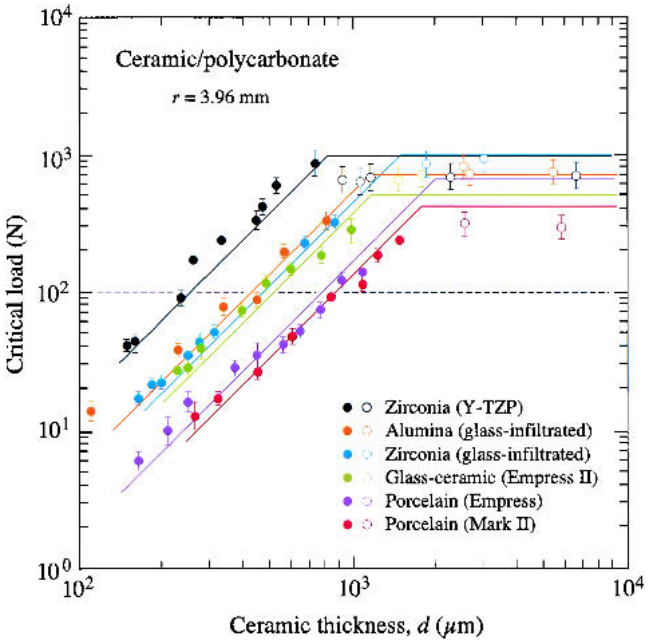

FIG. 9. Critical loads for onset of first damage in ceramic/polycarbonate bilayers as function of coating thickness *d,* for indentation with WC spheres ($r = 3.96$ mm).[15] Points are experimental data (standard deviation bars), filled symbols are P_R data, and unfilled symbols are P_C or P_Y data. Solid lines are theoretical predictions for radial (inclined lines) and cone cracking and quasiplasticity (horizontal lines). Dashed line is nominal operational load $P = 100$ N for dental function.

layers as a function of thickness *d,* for a fixed WC sphere radius $r = 3.96$ mm.[15] Data points are experimental results: at large *d* (unfilled symbols), either cone cracking or quasiplasticity, whichever occurs first (quasiplasticity in all cases in Fig. 9 except porcelain); at small *d* (filled symbols), radial cracking. Solid lines are corresponding predictions from Eqs. (1) and (2). Data in the radial cracking region appear to confirm a general P_R–d^2 dependence; however, there do appear to be some systematic tendencies toward lower slopes in some of the data sets (see below). The relative positions of the data sets for different materials reflect the material properties listed in Table I, especially the dependence of P_R on strength. Thus, Y-TZP zirconia is the most resistant to contact damage and glassy porcelains are the least resistant. Analogous tests for glass-coating layers on various substrates[85] confirm the dependence of P_R on modulus ratio E_c/E_s. Equations (1) and (2) may therefore be used to make *a priori* predictions for any ceramic-based bilayer from basic monolith properties, within an uncertainty of about a factor of two in critical load over two orders of magnitude in *d.*

Such plots provide sound guidelines for bilayer design.[3] For crack prevention, it is necessary to remain under the curves. Consider this requirement in relation to some specifiable operational load. In relation to dental function, a nominal biting force $P_m = 100$ N is indicated as the horizontal dashed line in Fig. 9. Safe design requires $P_R > P_m$ (especially) in Eq. (2), along with $P_C > P_m$ and $P_Y > P_m$ in Eq. (1) (with T_c and H_c replacing T and H). These conditions may be realized by maintaining a conservatively large sphere (cuspal) radius [recall r dependence in Eq. (1)] and coating thickness ($r > 5$ mm and $d > 1.5$ mm for example, depending on the ceramic). From the materials standpoint, one seeks to maximize the quantities T_c and H_c in Eq. (1) and σ_c in Eq. (2) (not always easily achieved simultaneously in any single ceramic), as well as to minimize E_c/E_s in Eq. (2). On the other hand, for crack containment it is necessary to maximize E_c/E_s, so as to maintain a soft (but tough) substrate for crack shielding and arrest. Accordingly, some compromise may be needed in the materials design.

2. Flaw statistics

Allusion was made to deviations from strict P_R–d^2 dependence of the data in Fig. 9 toward lower exponents. As mentioned, radial cracks initiate from flaws at the ceramic undersurface. These flaws are inevitably distributed in size and location, dependent on surface state (glasses) or immediately underlying microstructure (polycrystalline ceramics). Since the bell-shaped distribution of tensile stresses at the coating undersurface scales with *d* (Fig. 4), it can be hypothesized that the chance of locating a large flaw in the vicinity of the stress maximum should diminish as the coating becomes thinner. This would account for the reduced slopes in Fig. 9.

An appropriate flaw statistics analysis has been carried out.[86] Incorporation of stress gradient and flaw statistics functions into the critical load relation for radial cracks yields

$$P_R(d) = \int_0^\infty \left\{ \int_0^\infty f(P,R,d)\, dR \right\} \exp\left\{ -\int_0^P \int_0^\infty f(P',R,d)\, dR\, dP' \right\} P\, dP \quad , \tag{3}$$

where $f(P,R,d) = 2\pi r \rho S[c_*(P,R,d)]$, with ρ flaw density, c_* critical flaw size, $S(c)$ the probability density for any given flaw of size *c,* and *R* the radial location of a given flaw relative to the contact axis. The function $P_R(d)$ in Eq. (3) is compared with data for glass/polycarbonate bilayers in Fig. 10,[80] with ρ and $S(c)$ predetermined from digital image analysis of strength-controlling abrasion flaws (i.e., no adjustable parameters). The inclined line on the logarithmic plot is a prediction assuming crack initiation at the (size-independent) bulk strength, corresponding to an ideal P_R–d^2 response. Equation (3) gives a much better fit than the FEM prediction, with asymptotic overlap at large *d* and ever-widening deviations at small *d*. The latter deviations correspond to an effectively increasing coating

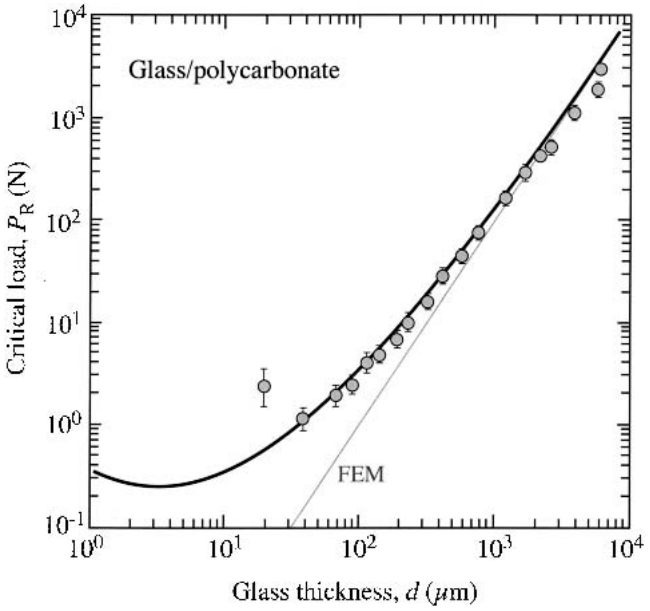

FIG. 10. Statistically-based $P_R(d)$ function for onset of radial cracks in glass/polycarbonate bilayers, indentation with WC spheres. Glass undersurfaces are preabraded to provide controlled flaw population. Points are experimental data (standard deviation bounds),[80] and solid curve is prediction from Eq. (3).[86] Inclined line is a FEM computation of idealized quadratic function in Eq. (2), for bulk glass strength 110 MPa.

strength σ_c in Eq. (2) with diminishing thickness d.[86] Again, in the thin-film region of very small d, the entire mode of damage may change, e.g., to concentric ring cracking mentioned earlier.[20,21] Transitions of this kind may be exacerbated by the higher stress gradients that exist over the starting flaws in thinner coatings, raising the issue of the validity of a simple critical stress condition for fracture. Such deviations may not be so evident in other tests, e.g., in more conventional flexural or tensile testing, or in thermal mismatch stress fields, where the stress gradients are smaller and large flaws thus more readily sampled.

Notwithstanding the modifying influence of flaw statistics in the thin-film region, Eq. (2) with averaged coefficients over the data range remains a valuable working relation for predicting responses of ceramic-based bilayer structures.

3. Rate effects

As noted in Sec. II, monolithic ceramics are susceptible to fatigue, most commonly from moisture-driven slow growth of cone cracks (but also from mechanical degradation of sliding interfaces within quasiplastic yield zones). In bilayers, radial cracks may be expected to undergo similar slow growth, especially if water gains access to the flaws in the coating undersurfaces (possibly from moisture in the epoxy bond). There is also potential for additional rate effects from deformation in soft substrates, e.g., viscoelasticity,[17,87] anelasticity,[88] or cumulative plasticity (or quasiplasticity).[89]

Such effects are readily quantified by measuring critical loads P_R in ceramic/polycarbonate bilayer specimens at different loading rates $\dot{P}$. Figure 11 plots $P_R(\dot{P})$ data for bilayers with glass and silicon coating layers.[43] The solid lines are best fits of the relation

$$P_R = [A(N+1)\dot{P}]^{1/(N+1)} \quad , \tag{4}$$

obtained by combining Eq. (2) with a stress intensity function ($K \sim \sigma c^{1/2}$) and conventional power law crack velocity function ($\upsilon \sim K^N$).[43] This plot is effectively the same as a conventional strength versus stressing rate ("dynamic fatigue") plot for ceramics, with N and A slope and intercept parameters in logarithmic coordinates. The values of exponent N determined from the fitted lines for both data sets are a little lower than those obtained from independent crack velocity determinations—silicon in particular is generally immune to slow crack growth (corresponding to $N = \infty$, i.e., zero slope). In these systems it is concluded that there is some extraneous, if minor, contribution from rate effects in the epoxy adhesive or polymeric substrate.

The data in Fig. 11 can be replotted as P_R versus time to failure t ($= P_R/\dot{P}$) on lifetime diagrams. On such plots the dynamic fatigue data overlap cyclic fatigue data from the same bilayers,[43] suggesting that there is no significant contribution to the radial crack growth in the glass and silicon from mechanical degradation.

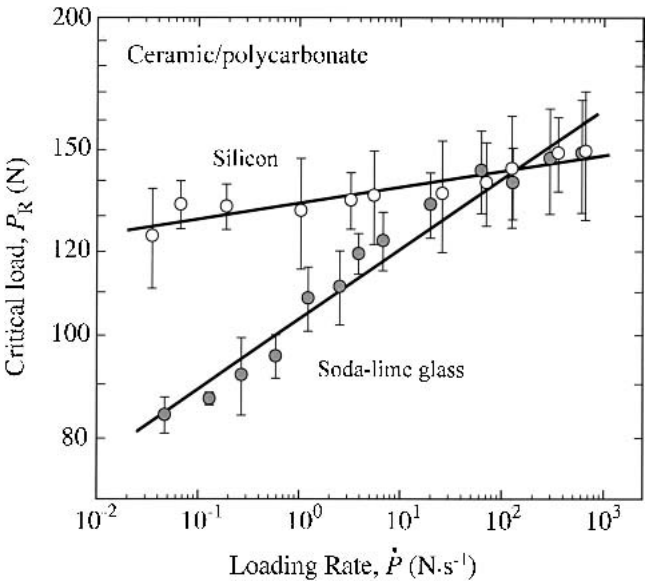

FIG. 11. Critical load P_R for radial cracking as function of loading rate $\dot{P}$ for coatings of soda-lime glass (filled symbols) and single-crystal silicon (unfilled symbols) bonded to polycarbonate substrates and subject to indentation with WC spheres.[43] Coating undersurfaces are abraded. Tests are in air (standard deviation bounds). Solid lines are best fits to Eq. (4).

4. Tangential loads

Thus far the discussion has been limited to normal contact loading. The question arises as to what role superposed lateral frictional loads, e.g., from an inclined or sliding contact, might play in the damage response of ceramic-based bilayers. In monoliths, tangential forces are known to have profound effects on local near-contact stress fields,[90,91] with consequent large reductions in surface critical loads P_C for cone cracking[92–94] and P_Y for yield.[66,95] Comparative studies of analogous effects on P_R in bilayer structures have not received the same attention in the literature.

Some recent experiments on glass/polycarbonate bilayers in contact loading at inclination angle α to the coating surface address this last issue.[96] This configuration imposes a tangential force P sin α onto a normal component P cos α, corresponding to a friction coefficient $\mu = \tan \alpha$. It is found that increasing α, while strongly reducing P_C, has no significant influence on P_R. Moreover, the axial location and starlike geometry of the radial cracks remain the same as in Fig. 7(b). This null result in the $P_R(\mu)$ dependence can be explained simply on grounds of symmetry. Basically, the superposition of surface tangential forces can be expected to enhance the tensile stresses behind the indenter and the compressive stresses ahead, with zero contribution to the pertinent out-of-plane normal stresses along the contact axis. Analogous experiments with sliding indenters show the same null result in $P_R(\mu)$—but in that case the radial cracks, once initiated, translate with the sliding indenter, increasing the prospect of material spallation and delamination failure.

We may conclude that the basic Hertzian test in normal loading remains a simple and powerful means of characterizing threshold conditions for radial fracture under any loading configurations, at least in flat-layer structures. More complex specimen geometries are better handled by FEM or simulation testers (e.g., mouth motion machines for dental crowns[33]).

5. Interlayer adhesives

In some layer structures a stiff coating layer may be joined by a soft adhesive to a stiff substrate to form a sandwich structure. The soft interlayer then facilitates crack arrest by deflection.[25,97–99] However, the same soft interlayer also allows flexure in the coating, enhancing the prospect of undersurface radial cracking, an important element in laminated windows.[87] Again, the notions of crack containment and crack prevention are in conflict.

Figure 12 shows P_R data for glass/epoxy/glass laminates as a function of epoxy adhesive interlayer thickness h, for selected coating thicknesses d (relatively thick glass support layers).[82] Note bounding cases: $P_R \to \infty$ at $h \to 0$ (fused interlayers, glass monoliths, zero flexure); $P_R \to P_\infty$ at $h \to \infty$ [brittle-coating/epoxy-substrate bilayer limit, Eq. (2)]. The data in Fig. 12 can be fitted to an empirical relation of form

$$P_R = P_\infty[1 + \beta(d/h)^\gamma] \quad , \tag{5}$$

with β and γ dimensionless constants. It is evident from Fig. 12 that even very thin adhesive layers ($h \ll d$) can facilitate significant flexure and attendant radial cracking in brittle coatings.

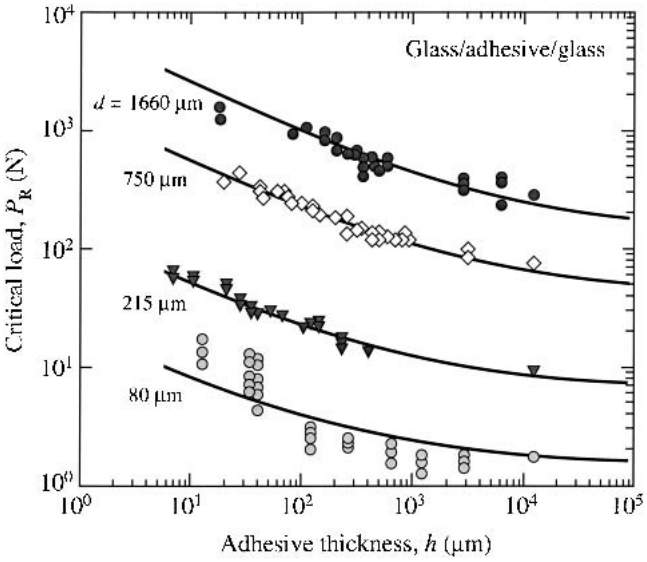

FIG. 12. Critical load P_R for radial cracking as function of adhesive thickness h for glass plates bonded to like glass substrates, for upper plate thicknesses d indicated. Data points are experimental results for specimens with bottom surface of glass overlayer abraded, with WC indenter; solid curves are empirical fits to Eq. (5).[82]

D. Fracture mechanics: Plastic substrates

In some bilayer systems the substrate may be stiffer than the ceramic coating ($E_s > E_c$) but may also be softer ($H_s < H_c$). This is often the case with metal [Fig. 5(b)] and tough ceramic [Fig. 5(c)] substrates. Contacts may then generate plasticity (or quasiplasticity) in the upper regions of the substrate, inducing local coating flexure above the yield zone. This flexure facilitates subsequent subsurface radial cracking in the coating. It follows that substrate yield is a necessary precursor to radial cracking in these systems, i.e., P_Y(substrate) < P_R(coating), so that P_Y becomes the controlling quantity.[79] This latter quantity is given to reasonable approximation in the point-loading limit ($a \ll d$) by

$$P_Y = GH_s d^2 \quad , \tag{6}$$

with $G = \alpha + \beta E_c/E_s$ a relatively slowly varying function and α and β dimensionless constants.[81]

Data for a porcelain/Pd–alloy bilayer system are shown in Fig. 13.[81] At low d, substrate yield (filled symbols) initiates first; at high d, cone cracks (unfilled

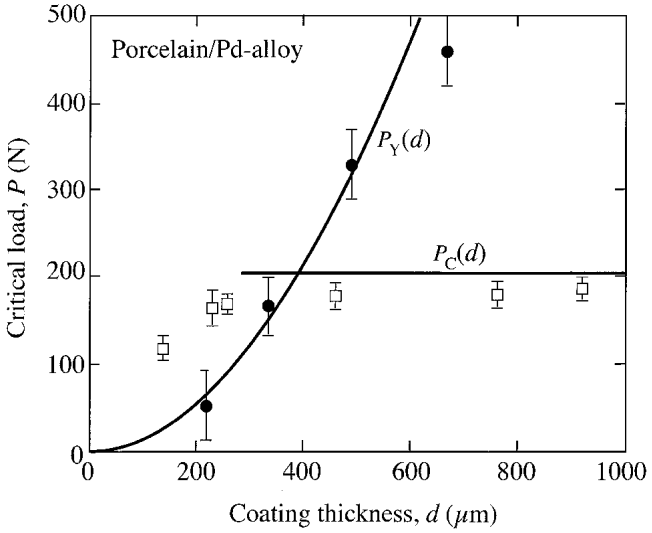

FIG. 13. Critical loads P_C and P_Y for porcelain/Pd–alloy bilayers as function of porcelain thickness d, indentation with WC spheres (r = 3.96 mm).[81] Points are experimental data (standard deviation bounds); filled symbols are P_Y data, and unfilled symbols are P_C data. Solid lines are theoretical predictions [Eq. (6) and (1a)].

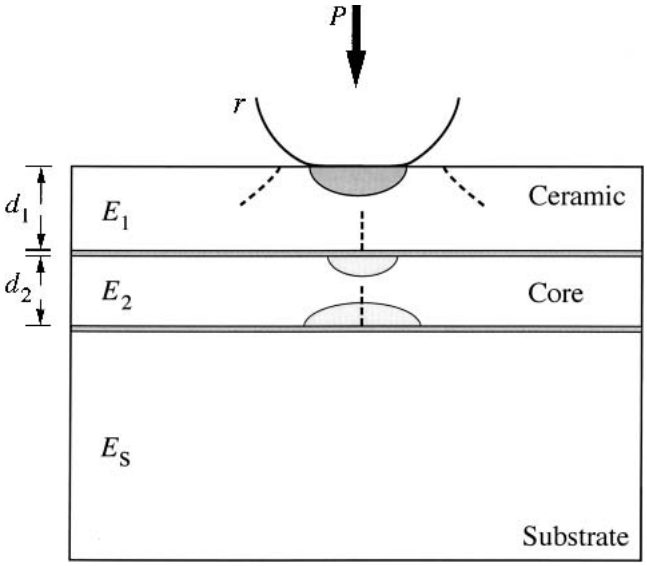

FIG. 14. Schematic of contact test with sphere on trilayer specimen with brittle outerlayer thickness d_1, core support layer (hard ceramic or metal) thickness d_2, on a compliant substrate (cf. Fig. 4). A radial crack (R) initiates preferentially at core lower surface, with cone cracking or quasiplastic yield at the veneer top surface. Yield can also occur in soft core layer, and radial cracking in veneer.

symbols) initiate first. The P_Y data are consistent with Eq. (6) (solid curve). From the standpoint of substrate design, the principal requirement is to maximize hardness H_s. (Increasing E_c/E_s is a secondary requirement.) On the other hand, once cracks do initiate, softer (and generally tougher) substrates are better equipped to arrest or inhibit any penetrant cracks within the sublayer,[30] so that design once more depends on whether crack prevention or crack containment is the more pressing goal.

IV. TRILAYERS

Now consider the trilayer system in Fig. 14, consisting of a bilayer coating of net thickness $d = d_1 + d_2$ on a compliant substrate, again subject to contact loading. The first layer is a ceramic for function or form, and the second layer is a strong or hard material for support. This is the basic structure of dental crowns, where an aesthetic porcelain veneer is fused onto a strong ceramic (e.g., glass-infiltrated alumina or zirconia) or a hard metal (e.g., Pd– or Co–alloy) core underlayer for cementation onto the remnant tooth structure.[34,37] The veneer ceramic remains susceptible to the same cone cracking and quasiplasticity modes at the upper surface and to radial cracking at the lower surface. However, the generally stiffer core layer, because it sustains the bulk of the flexural stresses from the applied loading, is also susceptible to fracture (ceramics) or yield (metals).

A. Ceramic-core trilayers

Figure 15 illustrates fracture in a model epoxy-bonded glass/sapphire/polycarbonate trilayer system,[41] in side view. This system is representative of all-ceramic porcelain/alumina/dentin crowns (compare material properties in Table I). The micrographs correspond to selective surface abrasion treatments: (a) top glass surface abraded, showing resultant formation of a shallow cone crack in the glass; (b) bottom glass surface abraded, showing formation of a radial crack in the glass; (c) bottom sapphire surface abraded, showing formation of a radial crack in the sapphire. Interestingly, the critical load for radial cracking in the sapphire is substantially lower than in the considerably weaker glass. FEM confirms that the tensile stresses are much higher in the sapphire layer and, further, that tensile stresses in the glass layer may be avoided altogether by eliminating any adhesive between the glass and sapphire, e.g., by fusing (recall Sec. III. C).[41] Thus, even though the sapphire is almost an order of magnitude stiffer and stronger than the glass, it is nevertheless most vulnerable. When they do occur, cracks remain contained within individual layers, illustrating once more the crack containment capacity in systems of large modulus mismatch.

If we regard the flexing ceramic bilayer as replaceable by an equivalent monolithic coating of thickness $d = d_1 + d_2$ and "effective modulus" $E_c^* = E_2 e(d_1/d_2, E_1/E_2)$, we may anticipate the relation for the critical load for core radial cracking to have a form analogous to Eq. (2); i.e.,

$$P_R = B^* \sigma_2 d^2 / \log(C E_c^*/E_s) \quad , \tag{7}$$

with σ_2 the strength of the core material and coefficient $B^* = Bb(d_1/d_2, E_1/E_2)$. Analytical expressions for $e(d_1/d_2, E_1/E_2)$ and $b(d_1/d_2, E_1 E_2)$ have yet to be established.

When such expressions become available, it will be possible to predict *a priori* the response of ceramic-based trilayer structures. Until then, one must resort to FEM or other numerical evaluation procedure, for predictions on a case-by-case basis.

Figure 16 plots critical loads P_R for glass/ceramic/polycarbonate trilayers as a function of core thickness d_2 (or glass thickness d_1), for fixed $d = 1.5$ mm (nominal dental crown thickness). Three relatively strong ceramic core materials are represented, glass–infiltrated alumina, lithium disilicate glass–ceramic, and Y-TZP (all surfaces polished). Solid curves are corresponding FEM predictions, using the materials data in Table I. The intersections of these curves with the right-hand axis at $d_2 = 1.5$ mm ($d_1 = 0$) correspond to limits for ceramic/polycarbonate bilayers with no veneer (cf. Fig. 9). For each trilayer system, P_R diminishes as more of the core is replaced by glass veneer. In the context of dental crowns, that is the price of aesthetics. However, P_R is higher in all regions than the level for glass/polycarbonate bilayers (horizontal dashed line in Fig. 16), confirming the effectiveness of the core support. The data are relatively insensitive to d_2/d_1 in the intermediate thickness region, so there is an inbuilt tolerance to variations in *relative* layer thickness (for the same reason that I-beams provide almost as much load-bearing capacity as solid beams—the material in the vicinity of the neutral axis of the

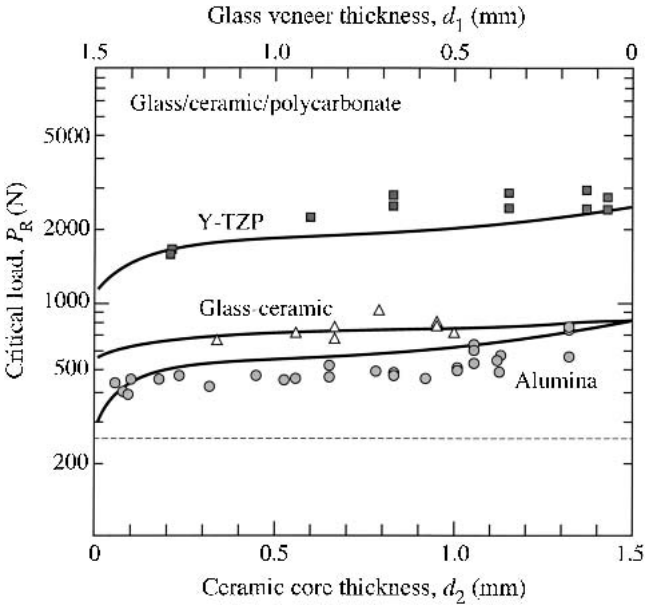

FIG. 16. Critical loads P_R for core radial cracking in glass/ceramic/polycarbonate trilayers, as a function of core ceramic thickness d_2 (lower axis) or glass thickness d_1 (upper axis), with net thickness $d = d_1 + d_2 = 1.5$ mm. Points are individual experimental data, and solid curves are FEM calculations. The horizontal dashed line is level for glass/polycarbonate bilayers (evaluated from bilayer data in Fig. 9).

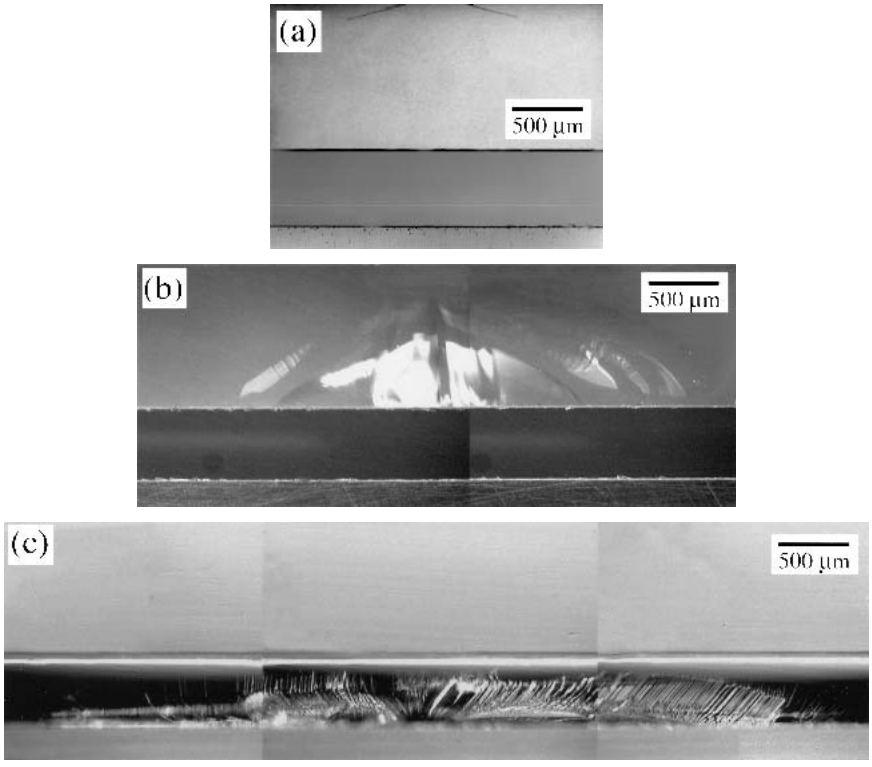

FIG. 15. Crack profiles in glass/sapphire/polycarbonate trilayer, $d_1 = 1$ mm and $d_2 = 0.5$ mm, after contact with WC sphere ($r = 3.18$ mm):[41] (a) cone crack in top-abraded glass surface, $P = 700$ N; (b) radial crack in bottom-abraded glass surface, $P = 800$ N; (c) radial crack in bottom-abraded sapphire surface, $P = 430$ N. Note containment of cracks within individual layers. (Micrographs are composites.)

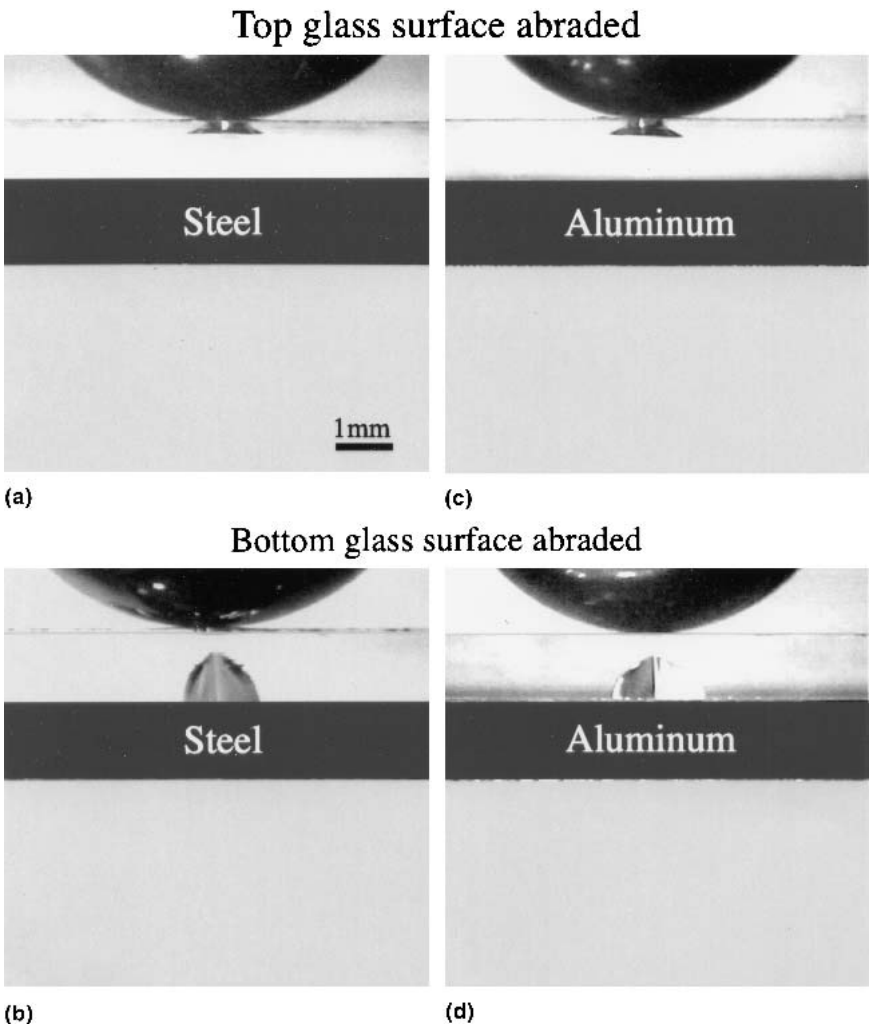

FIG. 17. *In situ* side-view micrographs showing crack initiation in epoxy-bonded glass/metal/polycarbonate trilayer, $d_1 = 1.2$ mm and $d_2 = 1.5$ mm, on polycarbonate substrate, indentation with WC sphere, $r = 3.96$ mm.[42] Steel core: (a) top glass surface abraded, showing cone crack at $P = 525$ N; (b) bottom glass surface abraded, showing radial crack at $P = 1210$ N. Aluminum core: (c) top glass surface abraded, cone crack at $P = 520$ N; (d) bottom glass surface abraded, radial crack at $P = 895$ N. (In the examples shown, radials are inclined to the plane of the figure.)

veneer/core flexing coating is under relatively little strain, so its properties in this region are of little consequence). Note, however, P_R remains sensitive to the *absolute* value of d in Eq. (7)—recall the elimination of radial cracks altogether in the bilayer limit $d_2 \rightarrow \infty$ [Fig. 5(d)].

Not shown in Fig. 16 are P_C values for cone cracking in the veneer top surface. The condition $P_C < P_R$ can become satisfied if the sphere (cuspal) radius is not large enough and if the core undersurface is relatively free of large flaws.[41]

B. Metal–core trilayers

One way to avoid core fracture is to replace the ceramic by a metal, as in traditional porcelain-fused-to-metal dental crowns. However, although not as brittle as ceramics, metals are nonetheless softer and can yield beneath the contact, resulting in flexure of the veneer overlayer. Such flexure is exacerbated if a soft bonding interlayer exists between the veneer and core support. Then radial cracking in the brittle outerlayer instead of in the core becomes a principal mode of failure. Of course, cone cracks may still occur at the top surface. Examples are shown in Fig. 17 for model glass/metal/polycarbonate trilayers with $E_2 > E_1$ but $H_2 < H_1$.[42] *In situ* side views of cracks in the glass are shown for steel and aluminum core metals: for top-surface-abraded glass, classical Hertzian cone cracks [Figs. 17(a) and 17(c)]; for bottom-surface-abraded glass layers, radial cracks [Figs. 17(b) and 17(d)]. Once more, the cracks remain wholly contained within the glass layers at initiation.

In analogy to Eq. (6) for bilayers, we may write the critical load for yield in the core metal layer in the simple form[81]

$$P_Y = G^* H_2 d^2 \quad . \tag{8}$$

For thick cores ($d_2 > d_1$), the location of first yield remains in the metal top surface [cf. Fig. 5(b)], with $G^* = (d_1/d)^2 G$ and $G = \alpha + \beta E_c^*/E_s$ (Sec. III. D). For thin cores ($d_2 < d_1$), the location of first yield shifts to the metal undersurface and $G^* = g(d_1/d_2, E_1/E_2)/\log(CE_c^*/E_s)$, i.e., closer in form to Eq. (7). The evolution of the plastic damage zones at different metal thicknesses has been mapped out for the systems in Fig. 17 using FEM.[81]

C. Design considerations

A conservative design strategy for trilayers is to select materials and relative layer thicknesses so as to avoid radial cracking (or any precursor plasticity) in either the core or veneer layers. (Recall that top surface damage can be avoided by ensuring a sufficiently blunt contact.) An outcome of Secs. A and B is that it is usually the core and not the veneer that is the weak link, even when the core is much stronger than the veneer. This is contrary to empirical wisdom in the dental literature, for instance, where the focus has been on strengthening the porcelain veneer. It follows that the critical loads P_R in Eq. (7) (ceramic cores) and P_Y in Eq. (8) (metal cores) should not diminish below the operational load. Simplistically, it might seem that these conditions could be ensured by making d sufficiently large, to minimize the flexural mode. However, this is not always possible because of functional constraints (e.g., crowns, $d < 1.5$ mm) or countervailing demands of crack containment, in which case it becomes necessary to optimize the individual layers. High-strength σ_2 (ceramics) and hardness H_2 (metals) would appear to be prime requirements. Veneer/core elastic modulus mismatch is also a factor, as may be seen from the data for alumina and glass–ceramic in Fig. 16: although P_R values for these two materials are similar at the bilayer limit $d_2/d = 1$, data for the stiffer alumina decline more rapidly as d_2/d declines.

Following Eqs. (7) and (8), it is instructive to construct design diagrams comparing P_R/d^2 and P_Y/d^2 versus d_1/d (or d_2/d) for selected high stiffness ceramic and metal cores. Figure 18 plots FEM-generated functions for porcelain fused to stiff alumina or Co–alloy cores, on dentin substrates. For alumina cores, $P_R(\text{core}) \ll P_R(\text{veneer})$ over the data range, highlighting the vulnerability of the brittle core. For Co–alloy cores, $P_Y(\text{core}) < P_R(\text{veneer})$ over the data range, confirming the precursor role of core yield in the veneer cracking. In this latter case, the kink in the P_Y curve at $d_1/d \approx 0.4$ corresponds to the transition in location of first yield from the top to the bottom core surface foreshadowed in Eq. (8).[42] [The inversion of the horizontal axes in Fig. 18 relative to Fig. 16 is simply to highlight the near-quadratic d_1 dependence of P_R in the thick-core region of Eq. (8).] Note that it is considerably easier to initiate radial cracks in the alumina trilayer than in the Co–alloy trilayer, except at $d_1/d < 0.25$. This would appear to indicate greater durability in metal-based

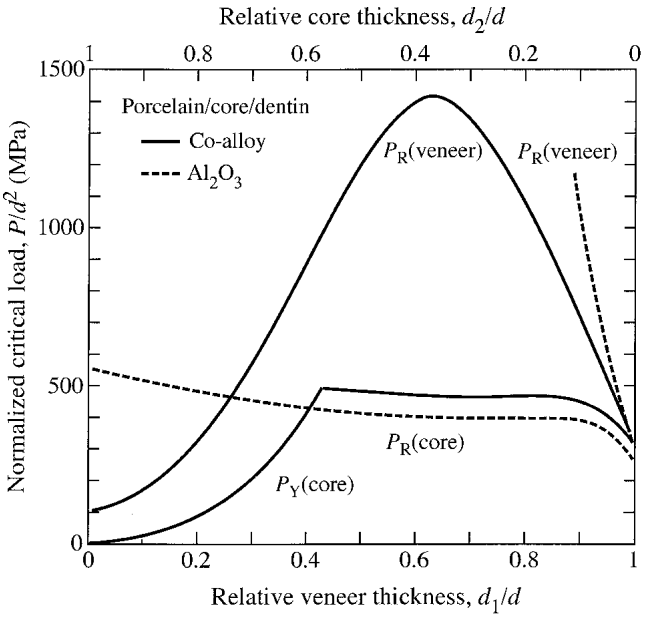

FIG. 18. FEM calculations of normalized critical loads P/d^2 for contact-induced subsurface damage in porcelain/core/dentin trilayers, for alumina (dashed curves) and Co–alloy (solid curves) as a function of d_1/d (or d_2/d). Plots are P_R to produce radial cracking, and P_Y to produce first yield at top ($d_1/d < 0.4$) and bottom ($d_1/d > 0.4$) surfaces.

trilayers, provided the veneer is not allowed to become too thin. On the other hand, premature yield in the metal cores may render the system vulnerable to fatigue, leading to altogether different modes of failure (e.g., delamination).[42]

There are trilayer configurations other than those represented in Fig. 18 that warrant attention. A case might be made for constructing systems with the stiffest, strongest, and hardest layer on top, to provide even greater protection to the underlayers. However, FEM calculations of sapphire/glass/polycarbonate trilayers[41] (cf. Fig. 15) indicate vulnerability to radial cracking in both core and veneer, with little or no increase in P_R and with reduced capacity to contain the cracks once they do initiate. All this is predicated on the absence of any soft interlayers between the adjoining stiff layers—as intimated in Fig. 12, any such interlayers will only increase the susceptibility to fracture in the veneer.

V. MULTILAYERS

Multilayers comprise the next degree of complexity. Mention was made of toughening by crack containment by deflection along weak interlayer interfaces in Sec. I. Brittle systems with soft interlayers provide the highest energy absorption, by restricting cracks to individual layers and by distributing the damage throughout the multilayer system. Some documented examples include the following: alumina/zirconia,[29] fine/coarse silicon nitride[31,100] and alumina[101] laminates; ceramic/metal laminates;[30] carbon fiber cross-ply composites;[102] glass/plastic laminates.[99,103–105]

Consider the system in Fig. 19, a laminate of n like brittle ceramic layers of thickness d and modulus E_c alternating with interlayers of thickness h ($<d$) and modulus E_i ($<E_c$), all bonded to a comparatively thick compliant substrate of modulus E_s ($<E_c$) and subjected to concentrated loading.[106] Incorporation of the interlayers may well confine any cracks that form in the brittle layers, by shielding adjacent layers;[11] however, these same interlayers may also make it easier to initiate the cracks in the first place, by enhancing flexural modes.[82] Our primary concern is with radial cracking at the brittle layer undersurfaces, at loads, $P_1, P_2, \ldots, P_n$ (although, again, cone cracking may occur at the outer brittle surface). The leading question then becomes: under what conditions is it structurally beneficial to replace a monolith coating of thickness D with an adhesively bonded laminate of n brittle layers each of thickness $d = D/n$. An optimum condition would appear to be $P_1/P_n = 1$, to avert premature radial cracking in the upper layers without compromising crack containment. A semiempirical extension of Eqs. (2) and (5) for radial cracking in the uppermost ceramic layer (layer 1) relative to that in the lowermost layer (layer n) has been derived for all-elastic systems[106]

$$P_1/P_n = (1/n^2)[1 + \beta(d/h)^{\gamma}] \\ [\log(CE_c/E_s)/\log(CE_c/E_i)] \quad , \qquad (9)$$

with β and γ dimensionless constants, subscripts *c, s,* and *i* denoting ceramic, substrate, and interlayer. Thus, to satisfy the compromise condition $P_1/P_n = 1$, it is necessary to adjust n, h/d, and E_c/E_i accordingly.

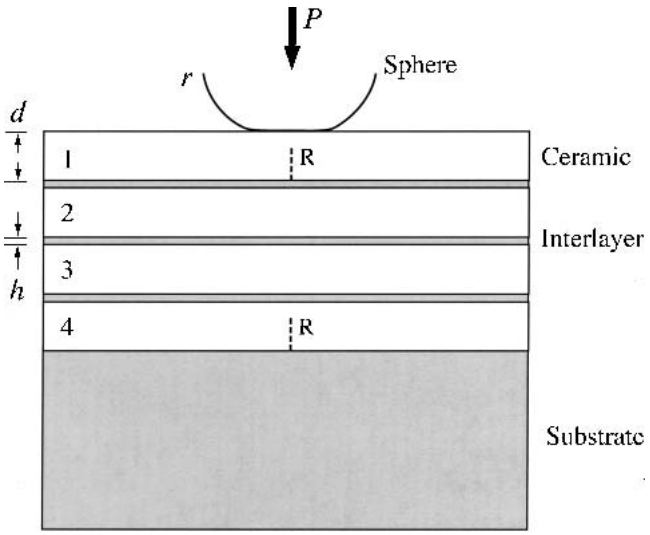

FIG. 19. Schematic of contact test with sphere on laminate of $n = 4$ brittle layers each with thickness d with compliant interlayer of thickness h, all bonded onto a compliant substrate, in contact with sphere at load P at the top surface. Radial cracks (and other damage modes) may initiate within any brittle layer (here depicted in layers 1 and 4), depending on relative layer thicknesses and material properties.

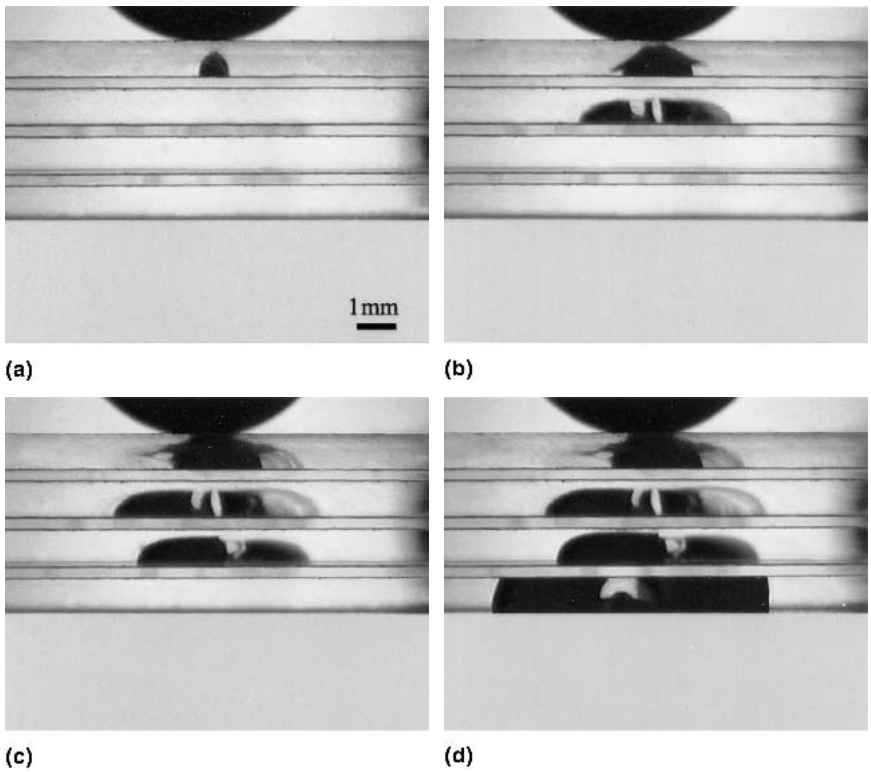

FIG. 20. Micrograph sequence for glass/polycarbonate laminate on polycarbonate substrates, $d = 1.0$ mm, interlayer thickness $h = 280$ μm, showing radial cracks in individual glass layers.[106] Load sequence: (a) $P = 230$ N; (b) $P = 850$ N; (c) $P = 1320$ N; (d) $P = 1370$ N. All glass undersurfaces are preabraded. [Note appearance of cone crack in the glass top layer in (b).]

A micrograph sequence for a model glass/polycarbonate multilayer system with $n = 4$ layers, bonded to a polycarbonate substrate ($E_s = E_i$), is shown in Fig. 20.[106] All the glass undersurfaces were preabraded, to ensure uniform flaw states. In this example, radial cracking appears first in the top layer, followed by sequential cracking in the successive layers. [A cone crack is evident in Fig. 20(b).] The radial cracks remain confined within each of the three top layers over the load range but penetrate through to the opposite surface in the bottom layer. At this last stage the structure is at the point of delamination at the weak interlayer interfaces, and hence of total failure. The damage tolerance of the structure is evident in the broad load range between the first and last cracks, $P_4/P_1 \approx 6$.

Similar laminates but with much smaller *h/d* show cracking in reverse order, i.e., bottom layer first and top layer last.[106] More complex structures may be contemplated, e.g., with thicker or stronger outerlayers to afford greater protection or graded layers to inhibit cone fracture.[107]

VI. CONCLUSIONS

The nature and mechanics of damage in brittle layer structures with compliant or soft underlayers under concentrated loads have been reviewed. Key damage modes have been identified and analyzed. Of these modes, radial cracking at the brittle layer undersurfaces is a principal source of failure, although cone cracking (or quasiplasticity) at the top (near-contact) surface remains a competing mode in all cases. Explicit relations for the critical loads to initiate each damage mode have been developed in terms of basic material properties and layer thicknesses. These provide working guidelines for predetermining optimum material combinations in applications where crack prevention is the basis of design, especially in biomechanical applications. Contact damage tests on model structures with transparent layers, in addition to more conventional sectioning observations, have been presented as experimental validation of such relations. Studies on bilayer, trilayer, and multilayer structures have been presented. The damage tolerance of such structures once cracks are initiated has been demonstrated.

ACKNOWLEDGMENTS

This study was supported by internal funds from the National Institute of Standards and Technology, University of Maryland, and Korea Advanced Institute of Science and Technology, and by grants from the U.S. National Institute of Dental and Craniofacial Research (Grant PO1 DE10976) and the Junta de Extremadura-Consejeria de Educacion Ciencia y Tecnologia y el Fondo Social Europeo of Spain (Grant IPR00A084).

REFERENCES

1. K.L. Johnson, *Contact Mechanics* (Cambridge University Press, London, U.K., 1985).
2. B.R. Lawn, J. Am. Ceram. Soc. **81,** 1977 (1998).
3. B.R. Lawn, K.S. Lee, H. Chaff, A. Pajares, D.K. Kim, S. Wuttiphan, I.M. Peterson, and X. Hu, Adv. Eng. Mater. **2,** 745 (2000).
4. B.R. Lawn, N.P. Padture, H. Cai, and F. Guiherteau, Science **263,** 1114 (1994).
5. D.F. Diao, K. Kato, and K. Hokkirigawa, Trans ASME J. Tribol. **116,** 860 (1994).
6. L. An, H.M. Chan, N.P. Padture, and B.R. Lawn, J. Mater. Res. **11,** 204 (1996).
7. S. Wuttiphan, B.R. Lawn, and N.P. Padture, J. Am. Ceram. Soc. **79,** 634 (1996).
8. A. Pajares, L. Wei, B.R. Lawn, and C.C. Berndt, J. Am. Ceram. Soc. **79,** 1907 (1996).
9. A.C. Fischer-Cripps, B.R. Lawn, A. Pajares, and L. Wei, J. Am. Ceram. Soc. **79,** 2619 (1996).
10. T.J. Lardner, J.E. Ritter, and G-Q. Zhu, J. Am. Ceram. Soc. **80,** 1851 (1997).
11. K.S. Lee, S. Wuttiphan, X.Z. Hu, S.K. Lee, and B.R. Lawn, J. Am. Ceram. Soc. **81,** 571 (1998).
12. K.S. Lee, S.K. Lee, B.R. Lawn, and D.K. Kim, J. Am. Ceram. Soc. **81,** 2394 (1998).
13. Y.G. Jung, S. Wuttiphan, I.M. Peterson, and B.R. Lawn, J. Dent. Res. **78,** 887 (1999).
14. Y-W. Rhee, H-W. Kim, Y. Deng, and B.R. Lawn, J. Am. Ceram. Soc. **84,** 1066 (2001).
15. Y. Deng, B.R. Lawn, and I.K. Lloyd, J. Biomed. Mater. Res. (Appl. Biomater.) **63,** 137 (2002).
16. A. Pajares, L. Wei, B.R. Lawn, N.P. Padture, and C.C. Berndt, Mater. Sci. Eng. A **208,** 158 (1996).
17. W.W. Gerberich, A. Strojny, K. Yoder, and L-S. Cheng, J. Mater. Res. **14,** 2210 (1999).
18. P.M. Ramsey, H.W. Chandler, and T.F. Page, Surf. Coat. Technol. **49,** 504 (1991).
19. M.V. Swain and J. Mencik, Thin Solid Films **253,** 204 (1994).
20. J.S. Wang, Y. Sugimura, A.G. Evans, and W.K. Tredway, Thin Solid Films **325,** 163 (1998).
21. A. Abdul-Baqi and E.V.d. Giessen, Int. J. Solids Struct. **39,** 1427 (2002).
22. S. Kamat, X. Su, R. Ballarini, and A.H. Heuer, Nature **405,** 1036 (2000).
23. R.Z. Wang, Z. Suo, A.G. Evans, N. Yao, and I.A. Aksay, J. Mater. Res. **16,** 2485 (2001).
24. J. Cook and J.E. Gordon, Proc. R. Soc. London A **282,** 508 (1964).
25. W.J. Clegg, K. Kendall, N.M. Alford, T.W. Button, and J.D. Birchall, Nature **347,** 455 (1991).
26. O. Prakash, P. Sarkar, and P.S. Nicholson, J. Am. Ceram. Soc. **78,** 1125 (1995).
27. R. Lakshminarayanan, D.K. Shetty, and R.A. Cutler, J. Am. Ceram. Soc. **79,** 79 (1996).
28. M.P. Rao, A.J. Sánchez-Herencia, G.E. Beltz, R.M. McMeeking, and F.F. Lange, Science **286,** 102 (1999).
29. D.B. Marshall, Am. Ceram. Soc. Bull. **71,** 969 (1992).
30. M.C. Shaw, D.B. Marshall, M.S. Dadkhah, and A.G. Evans, Acta Metall. **41,** 3311 (1993).
31. H. Liu, B.R. Lawn, and S.M. Hsu, J. Am. Ceram. Soc. **79,** 1009 (1996).
32. H.M. Chan, Annu. Rev. Mater. Sci. **27,** 249 (1997).
33. R. DeLong and W.H. Douglas, J. Dent. Res. **62,** 32 (1983).
34. J.R. Kelly, Annu. Rev. Mater. Sci. **27,** 443 (1997).
35. I.M. Peterson, A. Pajares, B.R. Lawn, V.P. Thompson, and E.D. Rekow, J. Dent. Res. **77,** 589 (1998).

36. Y-L. Tsai, P.E. Petsche, M.C. Yang, and K.J. Anusavice, Int. J. Prosthodont. **11,** 27 (1998).
37. J.R. Kelly, J. Prosthet. Dent. **81,** 652 (1999).
38. B.R. Lawn, Y. Deng, and V.P. Thompson, J. Prosthet. Dent. **86,** 495 (2001).
39. A.W. Eberhardt, J.L. Lewis, and L.M. Keer, ASME J. Biomed. Eng. **113,** 410 (1991).
40. G. Willmann, Adv. Eng. Mech. **3,** 135 (2001).
41. P. Miranda, A. Pajares, F. Guiberteau, F.L. Cumbrera, and B.R. Lawn, J. Mater. Res. **16,** 115 (2001).
42. H. Zhao, P. Miranda, B.R. Lawn, and X. Hu, J. Mater. Res. **17,** 1102 (2002).
43. C-S. Lee, D.K. Kim, J. Sanchez, P. Miranda, A. Pajares, and B.R. Lawn, J. Am. Ceram. Soc. **85,** 2019 (2002).
44. B.R. Lawn, *Fracture of Brittle Solids* (Cambridge University Press, Cambridge, U.K., 1993), Chap. 8 and 9.
45. A.C. Fischer-Cripps and B.R. Lawn, J. Am. Ceram. Soc. **79,** 2609 (1996).
46. B.R. Lawn and T.R. Wilshaw, J. Mater. Sci. **10,** 1049 (1975).
47. Y-W. Rhee, H-W. Kim, Y. Deng, and B.R. Lawn, J. Am. Ceram. Soc. **84,** 561 (2001).
48. I.M. Peterson, S. Wuttiphan, B.R. Lawn, and K. Chyung, Dent. Mater. **14,** 80 (1998).
49. F. Guiberteau, N.P. Padture, and B.R. Lawn, J. Am. Ceram. Soc. **77,** 1825 (1994).
50. H. Cai, M.A. Stevens Kalceff, and B.R. Lawn, J. Mater. Res. **9,** 762 (1994).
51. B.R. Lawn, N.P. Padture, F. Guibertea, and H. Cai, Acta Metall. **42,** 1683 (1994).
52. B.R. Lawn and D.B. Marshall, J. Mech. Phys. Solids **46,** 85 (1998).
53. B.R. Lawn, S.K. Lee, I.M. Peterson, and S. Wuttiphan, J. Am. Ceram. Soc. **81,** 1509 (1998).
54. K.S. Lee, Y-G. Jung, I.M. Peterson, B.R. Lawn, D.K. Kim, and S.K. Lee, J. Am. Ceram. Soc. **83,** 2255 (2000).
55. H. Cai, N.P. Padture, B.M. Hooks, and B.R. Lawn, J. Eur. Ceram. Soc. **13,** 149 (1994).
56. L. Wei and B.R. Lawn, J. Mater. Res. **14,** 939 (1996).
57. N.P. Padture and B.R. Lawn, J. Am. Ceram. Soc. **77,** 2518 (1994).
58. H.H.K. Xu, L. Wei, N.P. Padture, B.R. Lawn, and R.L. Yeckley, J. Mater. Sci. **30,** 869 (1995).
59. A. Pajares, L. Wei, B.R. Lawn, and D.B. Marshall, J. Mater. Res. **10,** 2613 (1995).
60. H. Cai, M.A.S. Kalceff, B.M. Hooks, B.R. Lawn, and K. Chyung, J. Mater. Res. **9,** 2654 (1994).
61. N.P. Padture and B.R. Lawn, J. Am. Ceram. Soc. **78,** 1431 (1995).
62. S.K. Lee and B.R. Lawn, J. Am. Ceram. Soc. **82,** 1281 (1999).
63. Y-G. Jung, I.M. Peterson, D.K. Kim, and B.R. Lawn, J. Dent. Res. **79,** 722 (2000).
64. F.B. Langitan and B.R. Lawn, J. Appl. Phys. **41,** 3357 (1970).
65. D.K. Kim, Y-G. Jung, I.M. Peterson, and B.R. Lawn, Acta Mater. **47,** 4711 (1999).
66. H.H.K. Xu, D.T. Smith, and S. Jahanmir, J. Mater. Res. **11,** 2325 (1996).
67. V.S. Nagarajan and S. Jahanmir, Wear **200,** 176 (1996).
68. H.H.K. Xu, S. Jahanmir, and L.K. Ives, J. Mater. Res. **11,** 1717 (1996).
69. F.C. Frank and B.R. Lawn, Proc. R. Soc. London A **299,** 291 (1967).
70. D. Tabor, *Hardness of Metals* (Clarendon, Oxford, U.K., 1951).
71. F.C. Roesler, Proc. Phys. Soc. Lond. B **69,** 981 (1956).
72. C. Kocer and R.E. Collins, J. Am. Ceram. Soc. **81,** 1736 (1998).
73. B.R. Lawn and D.B. Marshall, J. Am. Ceram. Soc. **62,** 347 (1979).
74. K.E. Puttick, J. Phys. D: Appl. Phys. **12,** L19 (1979).
75. B.R. Lawn, A.G. Evans, and D.B. Marshall, J. Am. Ceram. Soc. **63,** 574 (1980).
76. C.J. Russo, M.P. Harmer, H.M. Chan, and G.A. Miller, J. Am. Ceram. Soc. **75,** 3396 (1992).
77. L. Wei, A. Pajares, and B.R. Lawn, J. Mater. Res. **11,** 1329 (1996).
78. S. Wuttiphan, A. Pajares, B.R. Lawn, and C.C. Berndt, Thin Solid Films **293,** 251 (1997).
79. H. Zhao, X.Z. Hu, M.B. Bush, and B.R. Lawn, J. Mater. Res. **15,** 676 (2000).
80. H. Chai, B.R. Lawn, and S. Wuttiphan, J. Mater. Res. **14,** 3805 (1999).
81. H. Zhao, X. Hu, M.B. Bush, and B.R. Lawn, J. Mater. Res. **16,** 1471 (2001).
82. H. Chai and B.R. Lawn, J. Mater. Res. **15,** 1017 (2000).
83. H-W. Kim, Y. Deng, P. Miranda, A. Pajares, D.K. Kim, H-E. Kim, and B.R. Lawn, J. Am. Ceram. Soc. **84,** 2377 (2001).
84. S. Timoshenko and S. Woinowsky-Krieger, *Theory of Plates and Shells* (McGraw-Hill, New York, 1959), Chap. 8.
85. K.S. Lee, Y-W. Rhee, D.H. Blackburn, B.R. Lawn, and H. Chai, J. Mater. Res. **15,** 1653 (2000).
86. P. Miranda, A. Pajares, F. Guiberteau, F.L. Cumbrera, and B.R. Lawn, Acta Mater. **49,** 3719 (2001).
87. S.J. Bennison, A. Jagota, and C.A. Smith, J. Am. Ceram. Soc. **82,** 1761 (1999).
88. N. Iwashita, M.V. Swain, J.S. Field, N. Ohta, and S. Bitoh, Carbon **39,** 1525 (2001).
89. S. Suresh, *Fatigue of Materials* (Cambridge University Press, Cambridge, U.K., 1991).
90. G.M. Hamilton and L.E. Goodman, J. Appl. Mech. **33,** 371 (1966).
91. G.M. Hamilton, Proc. Inst. Mech. Eng. **197C,** 53 (1983).
92. B.R. Lawn, Proc. R. Soc. London A **299,** 307 (1967).
93. S-S. Chiang and A.G. Evans, J. Am. Ceram. Soc. **66,** 4 (1983).
94. B.R. Lawn, S.M. Wiederhorn, and D.E. Roberts, J. Mater Sci. **19,** 2561 (1984).
95. H.H.K. Xu and S. Jahanmir, J. Am. Ceram. Soc. **78,** 497 (1995).
96. C-S. Lee, B.R. Lawn, and D.K. Kim, J. Am. Ceram. Soc. **84,** 2719 (2001).
97. J.E. Gordon, *The New Science of Strong Materials* (Penguin, Harmondsworth, U.K., 1968).
98. C.A. Folsom, F.W. Zok, and F.F. Lange, J. Am. Ceram. Soc. **77,** 689 (1994).
99. C.A. Folsom, F.W. Zok, and F.F. Lange, J. Am. Ceram. Soc. **77,** 2081 (1994).
100. T. Ohji, Y. Shigegaki, T. Miyajima, and S. Kanzaki, J. Am. Ceram. Soc. **80,** 991 (1997).
101. H.C. Ha, H.M. Chan, and H.F. Nied, Acta Mater. **49,** 2453 (2001).
102. O. Jorgensen and A. Horsewell, Acta Metall. Mater. **8,** 3431 (1997).
103. A. Ball, Journal de Physique IV **7** C3921 (1997).
104. P.V. Grant, W.J. Cantwell, H. McKenzie, and P. Corkhill, Int. J. Impact Eng. **21,** 737 (1998).
105. I. Maekawa, H. Sudou, and K. Uda, Int. J. Impact Eng. **24,** 673 (2000).
106. H. Chai and B.R. Lawn, Acta Mater. **50,** 2613 (2002).
107. J. Jitcharoen, N.P. Padture, A.E. Giannakopoulos, and S. Suresh, J. Am. Ceram. Soc. **81,** 2301 (1998).